A ray-tracing technique for improving Satellite Laser Ranging atmospheric delay corrections, including the effects of horizontal refractivity gradients

G. C. Hulley[1] and E. C. Pavlis[2]

Received 3 November 2006; revised 2 March 2007; accepted 23 March 2007; published 23 June 2007.

[1] In this paper we study the effects of horizontal refractivity gradients on the propagation of optical signals for a globally distributed set of Satellite Laser Ranging (SLR) stations. Using two-dimensional ray tracing and globally distributed satellite data from NASA's Atmospheric Infrared Sounder (AIRS), as well atmospheric fields from the National Center for Environmental Prediction (NCEP), we calculate the effects of horizontal gradients on a global set of SLR stations using 2 years of data during 2004 and 2005. We investigate in detail how seasonal and diurnal changes, latitudinal dependence, topography, and oceans affect the gradients at specific locations, as well as the application of these gradients on a set of SLR data from the LAGEOS 1 and 2 geodetic satellites. For the year 2004, AIRS ray-tracing results showed maximum north-south (NS) gradient delays of 50 mm at 10° elevation angle at Herstmonceux, UK and east-west (EW) gradient delays of 35 mm at Yarragadee, Australia. Mean NS and EW gradients had delays not exceeding 5 mm for both AIRS and NCEP analysis at all stations. The standard deviations of AIRS gradients ranged from 6 to 12 mm, while NCEP gradients ranged from 3 to 9 mm, depending on location and time of year. The effects of applying AIRS and NCEP total ray-tracing results, including horizontal gradient contributions, to a set of global SLR geodetic data resulted in reduction of the solution residuals by up to 43% in variance percent difference. This is a highly significant contribution for the SLR technique's effort to reach an accuracy at the 1-mm level this decade.

Citation: Hulley, G. C., and E. C. Pavlis (2007), A ray-tracing technique for improving Satellite Laser Ranging atmospheric delay corrections, including the effects of horizontal refractivity gradients, *J. Geophys. Res.*, *112*, B06417, doi:10.1029/2006JB004834.

1. Introduction

[2] Atmospheric refraction is an important accuracy-limiting factor in the use of many space-based geodetic techniques such as Satellite Laser Ranging (SLR), Very Long Baseline Interferometry (VLBI), the Global Positioning System (GPS), and satellite altimetry, all of which suffer to a degree from limitations of current refraction models. SLR uses lasers (primarily at 532-nm wavelength) to measure very precise ranges from ground tracking stations to orbiting geodetic satellites with current single-shot accuracies at the subcentimeter level. The varying refractive index in the troposphere causes a delay in the propagation of the laser pulse, commonly known as the atmospheric or tropospheric delay.

[3] The current modeling of atmospheric refraction in the analysis of SLR data comprises the determination of the atmospheric delay in the zenith direction using an analytical formula driven by surface pressure, temperature and humidity, and subsequent projection to a given elevation angle, using an isotropic mapping function. Improved refraction modeling is essential in reducing errors in SLR measurements that study variations in the Earth's gravity field and crustal motion (especially for the vertical component), as well as monitoring sea level rise, precise orbit determination, post-glacial rebound, and other geophysical phenomena. In most of these applications, and particularly for the establishment and monitoring of the International Terrestrial Reference Frame (ITRF) [*Altamimi et al.*, 2002], of great interest is the stability of its scale and its implied height system. A new zenith delay model (M-P model) developed by *Mendes and Pavlis* [2004], is now the adopted standard for refraction modeling and is valid for a wide spectrum of wavelengths (355–1064 nm) with submillimeter accuracies. New mapping functions (FCULa and FCULb) developed by *Mendes et al.* [2002] have a 2-year-average RMS (model minus ray tracing through radiosonde data) of approximately 7 mm at 10° elevation.

[4] However, these are still models that are formulated by assuming an unrealistic spherically symmetric atmosphere,

[1]Joint Center for Earth Systems Technology, University of Maryland Baltimore County, Baltimore, Maryland, USA.
[2]Joint Center for Earth Systems Technology, NASA Goddard Space Flight Center, Greenbelt, Maryland, USA.

Copyright 2007 by the American Geophysical Union.
0148-0227/07/2006JB004834$09.00

and hence there are no contributions to the delay from horizontal refractivity gradients around the SLR tracking sites. In order to improve models of atmospheric delay, horizontal gradients in the atmospheric refractive index still need to be modeled and researched on a global scale. In the past, GPS and VLBI groups have calculated refractivity gradients from the geodetic data measurements and by using meteorology fields such as NCEP (National Center for Environmental Prediction) [see, e.g., *Chen and Herring*, 1997; *MacMillan and Ma*, 1997]. Estimating gradients from the GPS and VLBI geodetic data is possible since the observing session views multiple targets simultaneously in various directions around the station down to 3° elevation, and in the case of GPS in particular, this process is continuous. On the other hand, SLR gradient estimation is not possible since a SLR system can only observe one target at a time and down to a minimum elevation angle of 10° (due to eye-safety concerns). Furthermore, with only a few targets available (the two LAGEOS and the two ETALON satellites), we only have the ability to track one pass, rarely two per day, and the tracking lasts at best between 30 and 40 min for a zenith pass, which seldom occurs, and is often between 10 and 20 min on average. Consequently, the only way to estimate horizontal gradients for SLR purposes is by using a ray-tracing technique or a gradient delay model.

[5] We are now entering a new era where global snapshots are available from satellite-borne instruments on a daily basis, and we will be using atmospheric profiles from the Atmospheric Infrared Sounder (AIRS) instrument on NASA's AQUA Earth Observing System (EOS) platform to perform the ray tracing and to compute the atmospheric delay, including horizontal refractivity gradients, at any elevation and azimuth angle around any particular SLR station.

2. Horizontal Refractivity Gradients

2.1. Background

[6] The assumption made by all current atmospheric delay models of a spherically symmetric atmosphere is inherently flawed as it does not take into account the presence of azimuthal asymmetries in the atmosphere. We have found that the contribution of horizontal gradients to the total atmospheric delay can reach the few-centimeter level at 10° elevation. Although centimeter delay corrections may seem small, horizontal gradients still need to be taken into account since they can lead to systematic errors in estimated vertical and horizontal station coordinates, which in turn affect the accuracy of the scale and origin of the ITRF. Ignoring horizontal gradients is most likely the largest source of error in current atmospheric delay models for SLR at low-elevation angles. Ranging at the lowest elevation possible is required in order to decorrelate system errors in the ranging system and the station's height.

[7] Recent studies of atmospheric gradients by *MacMillan* [1995], *Chen and Herring* [1997], *MacMillan and Ma* [1997], and *Boehm and Schuh* [2006] were all focused on their impact on the analysis of VLBI geodetic data at radio wavelengths. *Chen and Herring* [1997] found north-south (NS) gradients with average values of up to 20 mm of delay when averaged over a month and for an elevation angle of 10°. An RMS of 5–10 mm was typically found at midlatitude sites. The gradients were calculated from three-dimensional weather analysis fields from NCEP and provided good agreement between gradients estimated using VLBI data. Earlier studies at optical wavelengths by *Gardner* [1977], *Gardner et al.* [1978], and *Abshire and Gardner* [1985] found gradient delays of up to 30 mm at 10° elevation using radiosonde data from eight locations around Leonardtown, Maryland during January and February 1970. As of now, the effects of horizontal gradients on the analysis of SLR data at optical wavelengths and on a global scale have not been investigated in detail.

2.2. Atmospheric Delay Formulation

[8] The optical path length between the tracking station and satellite is defined as the integral of the group refractive index along the path of the ray. The geometry of the raypath traveling through the atmosphere to the satellite is shown in Figure 1. We define the atmospheric delay as the difference between the optical path length and the geometric path length as follows:

$$d_{\mathrm{atm}} = \int_{\mathrm{ray}} n\,\mathrm{d}s - \int_{\mathrm{vac}} \mathrm{d}s \tag{1}$$

where n is the group refractive index, and $\mathrm{d}s = \mathrm{d}r/\sin\theta$ is a differential element of length along the path of the ray. The subscripts "ray" and "vac" in the integral indicate the actual raypath and vacuum path of the signal. If we express the group refractive index in terms of the group refractivity N,

$$n = 1 + 10^{-6}N \tag{2}$$

then the atmospheric delay can be expressed as

$$d_{\mathrm{atm}} = 10^{-6}\int_{\mathrm{ray}} N\mathrm{d}s + \left[\int_{\mathrm{ray}} \mathrm{d}s - \int_{\mathrm{vac}} \mathrm{d}s\right] \tag{3}$$

where the first term is the excess path delay or velocity error, and the bracketed term is the delay due to the bending of the ray, called the geometric delay (d_{geo}). At optical wavelengths, and for a site at sea level, the delay in the zenith direction is approximately 2.5 m and can reach values of up to 14 m for an elevation angle of 10°. The geometric delay is only significant at low-elevation angles and typically has values of around 2 cm at 10° elevation.

[9] The International Association of Geodesy (IAG) [*International Union of Geodesy and Geophysics*, 1999] currently recommends that the group refractivity for visible and near-infrared wavelengths be computed using procedures described by *Ciddor* [1996] and *Ciddor and Hill* [1999]. Following the work of *Mendes and Pavlis* [2004], the group refractivity for the hydrostatic (N_{h}) and non-hydrostatic (N_{nh}) components are given by:

$$N_{\mathrm{h}} = K_1^L f_{\mathrm{h}}(\lambda) Z_d R_d \left(\frac{P}{T} - (1-\epsilon)\frac{e}{T}\right) \tag{4}$$

$$N_{\mathrm{nh}} = -K_1^L \epsilon f_{\mathrm{h}}(\lambda)\left(\frac{Z_{\mathrm{d}}}{Z}\right)\left(\frac{e}{T}\right) + K_2^L f_{\mathrm{nh}}(\lambda)\left(\frac{Z_{\mathrm{w}}}{Z}\right)\left(\frac{e}{T}\right) \tag{5}$$

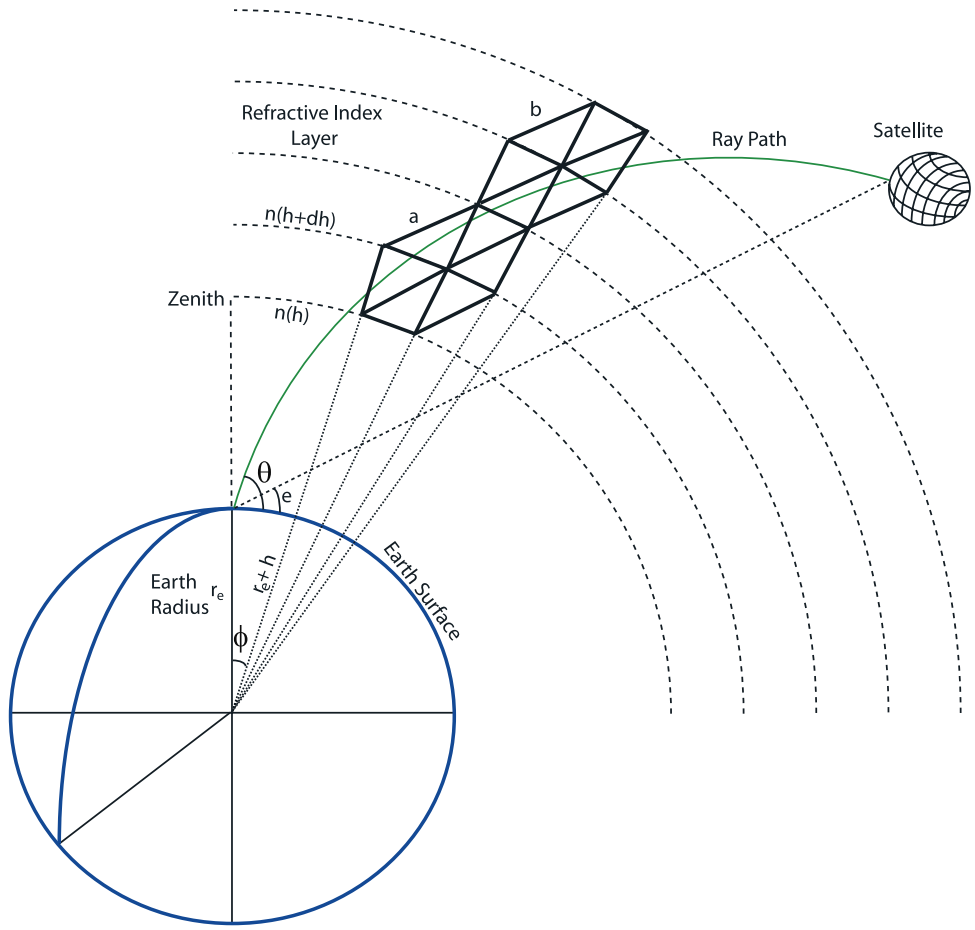

Figure 1. Schematic showing the geometry of the raypath between the tracking station and satellite. Where r_e is the radius of the Earth; $n(h)$ is the refractive index layer at height, h, and $n(h + dh)$ is the refractive index layer at height $h + dh$; θ is the elevation angle of the raypath; e is the elevation angle of the vacuum path; ϕ is the geocentric radius angle; a and b are examples of two data grid cells at height h and $h + dh$ that the ray passes through.

where $K_1^L = 0.8239568$ K Pa^{-1}, $K_2^L = 0.7247600$ K Pa^{-1}, $\epsilon = \frac{M_w}{M_d}$, where M_d is the molar mass of dry air and M_w is the molar mass of water vapor, Z, Z_d, and Z_w are the compressibility factors for moist air, dry air, and pure water vapor and are needed in order to account for departures of dry air and water vapor from ideal gas behavior, T is the temperature (K), P is total pressure (Pa), e is the water vapor pressure (Pa), and $f_h(\lambda)$ and $f_{nh}(\lambda)$ are the hydrostatic and nonhydrostatic dispersion equations as follows:

$$f_h(\lambda) = 10^{-2}\left[k_1^* \frac{(k_0+\sigma^2)^2}{(k_0-\sigma^2)^2} + k_3^* \frac{(k_2+\sigma^2)^2}{(k_2-\sigma^2)^2}\right] C_{CO_2} \quad (6)$$

$$f_{nh}(\lambda) = 0.003101(w_o + 3w_1\sigma^2 + 5w_2\sigma^4 + 7w_3\sigma^6) \quad (7)$$

where the k and w coefficients are given in Table 1, and $\sigma = 1/\lambda$ where λ is the wavelength of the laser pulse.

[10] In order to compute the total atmospheric delay, including the contribution from horizontal refractivity gradients, we expand the refractivity N in a Taylor's series expansion around the laser site [*Gardner*, 1977] as follows:

$$N(r,\rho) = N(r) + \rho\frac{\partial}{\partial\rho}N(r)|_{\rho=0} + \frac{\rho^2}{2!}\frac{\partial^2}{\partial\rho^2}N(r)|_{\rho=0} + \ldots \quad (8)$$

where ρ represents horizontal distance from the laser site, r is the radial distance from the Earth's center, and $N(r)$ is the radially dependent refractivity above the site. The

Table 1. Dispersion and Compressibility Coefficients

Coefficient	Value	Units
k_o	238.0185	μm^{-2}
k_2	57.362	μm^{-2}
k_1^*	19,990.975	μm^{-2}
k_3^*	579.55174	μm^{-2}
ω_o	295.235	unitless
ω_1	2.6422	μm^2
ω_2	−0.032380	μm^4
ω_3	0.004028	μm^6

gradient delay is estimated from the first-order term in equation (8). The delay contribution from the higher-order terms is negligible, and we have calculated values at the 10^{-5}-mm level at 10° elevation.

[11] The refractivity in terms of the Earth-centered spherical coordinates, using only the first two terms in equation (8), can then be expressed as [*Chen and Herring*, 1997]

$$N(r, \alpha, \phi) = N(r) + N_{\mathrm{ns}}(r)\rho\cos\alpha + N_{\mathrm{ew}}(r)\rho\sin\alpha \qquad (9)$$

where $\rho = r\phi$ represents horizontal arc distance, α is the azimuth angle, ϕ is the angle from the center of the Earth, and N_{ns} and N_{ew} are the north-south (NS) and east-west (EW) components, respectively, of the horizontal refractivity gradient ($N_{\mathrm{ns}} = \frac{\partial}{\partial\rho}N(r)\hat{\mathrm{n}}\mathrm{s}$, $N_{\mathrm{ew}} = \frac{\partial}{\partial\rho}N(r)\hat{\mathrm{e}}\mathrm{w}$). The cos α and sin α terms give the projection of the NS and EW gradient on the azimuth of the observation.

[12] By substituting equation (9) into equation (3), the total atmospheric delay, including gradients, can be written as follows:

$$d_{\mathrm{atm}} = 10^{-6}\int_{r_{\mathrm{s}}}^{r_{\mathrm{a}}}\frac{N(r)}{\sin\theta}\mathrm{d}r + d_{\mathrm{geo}} + \left[\int_{r_{\mathrm{s}}}^{r_{\mathrm{a}}}\frac{N_{\mathrm{ns}}(r)\rho}{\sin\theta}\mathrm{d}r\right]\cos\alpha + \left[\int_{r_{\mathrm{s}}}^{r_{\mathrm{a}}}\frac{N_{\mathrm{ew}}(r)\rho}{\sin\theta}\mathrm{d}r\right]\sin\alpha \qquad (10)$$

where θ is the elevation angle at the altitude calculated using Snell's law, r_{s} is the geocentric radius of the station, and r_{a} is the geocentric radius at the top of the atmosphere. In this paper, NS gradients are calculated from north to south, and EW gradients are calculated from west to east. The NS and EW gradient delays are calculated by numerically integrating the third and fourth terms in equation (10) using a ray-tracing algorithm.

3. Ray Tracing

[13] The total atmospheric delay can be evaluated by numerically integrating equation (10) along the path of a laser pulse starting at the surface and passing through the atmosphere to a geodetic satellite such as LAGEOS 1 or 2. The signal passes through layers of varying refractive index due to pressure and temperature variations that result in the pulse speeding up as it passes through regions of lower density. The signal also follows a curved path due to ray bending, a consequence of Snell's law. The ray-tracing computation process is based on geometric optics theory applied over a series of thin spherical shells until the top of the atmosphere. A constant refractivity is assumed within each spherical shell. The NS and EW components of the horizontal gradient delay [third and fourth terms in equation (10)] can be evaluated directly by integrating values at each spherical shell layer i until the top of the atmosphere (TOA) as follows:

$$d^i_{\mathrm{ns}} = 10^{-6}\frac{N^{\mathrm{l}}_{\mathrm{ns}} + N^{\mathrm{u}}_{\mathrm{ns}}}{2}\rho\mathrm{d}s \qquad (11)$$

$$d^i_{\mathrm{ew}} = 10^{-6}\frac{N^{\mathrm{l}}_{\mathrm{ew}} + N^{\mathrm{u}}_{\mathrm{ew}}}{2}\rho\mathrm{d}s \qquad (12)$$

where d^i_{ns} and d^i_{ew} are the delays in the NS and EW directions for level i, ρ is the horizontal position coordinate measured from the station location, ds is the integration step size, and l and u specify the lower and upper boundaries of layer i.

3.1. AIRS

[14] The Atmospheric Infrared Sounder (AIRS) is one of many instruments aboard AQUA, a polar orbiting satellite that is part of the NASA-centered Earth Observing System (EOS) used for climate research and weather prediction (for detailed information, see http://disc.gsfc.nasa.gov/AIRS/documentation.shtml). AIRS is a hyperspectral infrared instrument that measures the radiance that reaches the top of the atmosphere at a given frequency. The conversion of the measured quantity (radiance) into a geophysical quantity (temperature, humidity, etc.) is called a retrieval and is an inverse problem that needs to be solved in the most optimal way possible. A significant advantage of AIRS is that it uses 2378 spectral channels to measure a broad range of wavelengths, as compared to earlier instruments that only used 15 channels. The higher number of channels results in measurements that are of higher sensitivity, precision, and accuracy. A further advantage of using AIRS is that it provides rapid and global coverage of the Earth and the data is available at almost near real time.

[15] AIRS data coverage is pole-to-pole, and the Earth is covered twice daily consisting of a descending (daytime) and an ascending (nighttime) path. Ascending and descending orbits do not cover the same area of the Earth. The data is retrieved in the form of a granule which contains 6 min of data and is approximately 2300 (NS) km × 1600 (EW) km in spatial extent with a 50-km horizontal resolution within the granule. One day of data yields 240 granules. We use AIRS level 2 support product (V4.0) profiles of temperature, pressure, and water vapor at 100 standard pressure levels extending from 1100 up to 0.1 mb.

[16] In order to perform the ray tracing, three-dimensional atmospheric grids need to be constructed around each operational SLR tracking station. The data is first processed and then grouped into 10° × 10° latitude/longitude grids with a 0.5° spatial resolution and up to an altitude of 0.1 mb. In this way, rays with elevation angles above 5° will remain in the three-dimensional atmospheric grid to an altitude of 45 km. From now on we will refer to AIRS ray-tracing results as ART.

3.2. NCEP/NCAR Reanalysis Data

[17] In addition to the AIRS results, we use NCEP/NCAR reanalysis fields [*Kalnay et al.*, 1996] from the Climate Data Assimilation System (CDAS) to make comparisons over the same time period and station locations. The current CDAS data is geared toward using satellite data, and computer capacities are geared to accommodate this data. The reanalysis project is supported by the National Oceanic and Atmospheric Administration's (NOAA) Office of Global Programs. NOAA's main computing facility in Gaithersburg, Maryland receives over 123 million satellite observations per day and, using computational speeds of 1.485 trillion calculations per second combined with advanced global, regional, and hazard models, results in significant advances in weather forecasting and climate prediction. Examples of

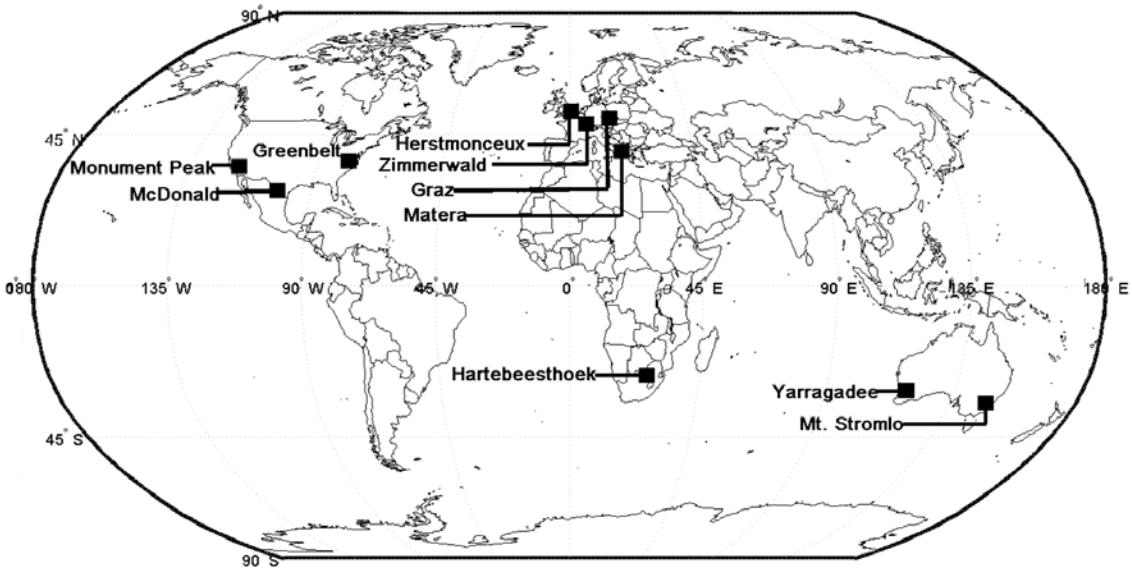

Figure 2. SLR Station locations.

current satellite data used in the NCEP numerical weather models used are as follows: GOES, AMSU, Quickscat, AIRS, MODIS, and TOVS. *Mo et al.* [1994] and, more recently, *Thépaut* [2003] discussed in detail the benefits and effects of incorporating satellite data into numerical weather models. The NCEP reanalysis global fields we use contain four files per day, at 00, 06, 12, and 18 h UTC with data given on a 2.5° latitude/longitude grid and with 17 standard pressure levels in the atmosphere until 10 mb. The variables used to build the three-dimensional refractivity profiles are geopotential height, temperature, pressure, and relative humidity. We will refer to the results from NCEP ray-tracing as NRT from this point on.

3.3. Factors Affecting Gradient Variations

[18] Under stable atmospheric conditions, surface pressure is relatively uniform, and as a result, we expect that the horizontal refractivity gradients will primarily be a function of temperature gradients [*Gardner*, 1977]. For the majority of our observations we find this to be true; however, we also find that cold fronts and undulating terrain features such as mountains will result in large horizontal pressure gradients. Diurnal changes will primarily effect the EW component of the gradient in that temperatures fluctuate from being warmer in the east during the morning hours, resulting in positive EW gradients, to being warmer in the west during the evening hours, resulting in negative EW gradients. For the majority of stations and in both NS and EW components we found that the refractivity gradients were larger during the day than at night.

[19] On a global scale, refractivity will increase from the equator to the poles due to the systematic decrease in surface temperature away from the equator. As a result we should see primarily negative NS refractivity gradients in the Northern Hemisphere and positive NS refractivity gradients in the Southern Hemisphere. Our results in Table 4 in fact show that all the Northern Hemisphere sites have negative mean NS gradients, with larger values at midlatitude sites such as Herstmonceux, Graz, and Zimmerwald. In the Southern Hemisphere, Hartebeesthoek and Mt. Stromlo have positive NS mean gradient values, but Yarragadee shows a preferred negative direction in the NS gradient component. However, large standard deviations at most of the sites indicate that the NS gradients fluctuate and can be highly variable throughout the year. This is most likely due to the fact that temperature variations around the stations occur on the mesoscale, resulting in the gradients being primarily a function of local terrain features such as large bodies of water, topography, and vegetative cover, as opposed to the equator-to-pole temperature decrease.

[20] We have found significant fluctuations in the gradient delay due to seasonal changes. The seasonal fluctuations are more noticeable when stations are situated near the ocean, resulting in large land-water temperature differences during the summer months. Also, during the warmer months, the temperatures in the boundary layer are more unstable due to convection, and as a result, we find that the temperature gradients are more variable at stations situated near sea level. Larger NS gradient variations were found during the winter months at Herstmonceux, UK indicating frequent changes in weather patterns during this period and location.

4. AIRS Results and Analysis

[21] We chose 10 of the most significant (in terms of data yield and length of historical record), globally distributed International Laser Ranging Service (ILRS) tracking stations to perform our analysis (see Figure 2 and Table 2). Table 4 displays the mean and standard deviation of the NS and EW gradient delays at 10° elevation during 2004 and 2005 for all stations at a wavelength of 532 nm. The mean delays do not exceed 5 mm in absolute magnitude, with corresponding standard deviations between 6 and 12 mm. We have found that the contribution of horizontal gradients to the total atmospheric delay can reach the few-centimeter level at 10° elevation and can be as large as 5 cm at certain locations (where SLR stations operate) and times of year. We observed similar trends in gradient direction, magnitude, and variation

Table 2. Information for the 10 SLR Stations Used in This Analysis

Station	Country	Latitude	Longitude, °E	Height, m
HX, Herstmonceux	UK	50.9	0.3	75
GR, Graz	Austria	47.0	15.5	495
ZM, Zimmerwald	Switzerland	46.9	7.5	951
MA, Matera	Italy	40.7	16.7	537
GR, Greenbelt	USA	39.0	283.3	19
MP, Monument Peak	USA	32.9	243.6	1837
MD, McDonald	USA	30.7	256.0	2006
HH, Hartebeesthoek	South Africa	−25.9	27.7	1407
YA, Yarragadee	Australia	−29.0	115.3	244
MS, Mt. Stromlo	Australia	−35.2	149.0	805

from the 2004 and 2005 results, and as a result, we calculate gradient statistics for a 2-year period. We do, however, show a year-to-year comparison for Herstmonceux and Yarragadee in Table 3.

[22] In order to investigate what type of seasonal gradients to expect during the year, Figures 3 and 4 show NS (0° azimuth) and EW (90° azimuth) gradient delays at 10° elevation for 2004 at Herstmonceux and Yarragadee using ART and NRT results. Figures 5 and 6 show NS and EW refractivity gradient profiles at Yarragadee and Monument Peak during February and August 2004. By holding either the horizontal temperature or pressure fields constant at all levels through which the ray traverses, it is possible to separate out contributions from these two variables to the total gradient delay. For example, we can set the temperatures constant at each level resulting in horizontal pressure and water vapor pressure gradients being the only contributions to the delay. Since the water vapor pressure (wet) contribution is negligible, we can investigate which variable (temperature or pressure) has the largest contribution to the total gradient delay. In Figures 5 and 6 we distinguish between the total gradient (solid line) and separate contributions from pressure (dotted line) and temperature (dashed line) gradients. The profiles give the mean values of the gradients at each level for the entire month and are multiplied by a factor of 10^5 for plotting purposes. Table 5 shows the equivalent gradient delay values for each contribution (Total, Pressure, and Temperature) at Monument Peak and Yarragadee.

[23] Table 6 shows diurnal and seasonal variations at four stations (Yarragadee, Herstmonceux, Monument Peak, and Zimmerwald) for a 2-year period (2004 and 2005) using ART at 10° elevation. For the Northern Hemisphere sites, summer statistics are for the time period from April to September and winter statistics are from October to April. At Yarragadee, summer statistics are from November to March and winter statistics are from April to November. Since AIRS orbits the globe twice daily, there are possibly two AIRS granules that can be used per day at each station. For example, at Yarragadee, we obtain two granules per day, a daytime granule at 05 UTC and a nighttime granule at 17 UTC. The corresponding day-night gradient delay values are shown in Table 6.

[24] We now analyze our gradient results at four stations in more detail. The stations chosen for the analysis are the most reliable in the ILRS network since they produce the most data (normal points). They also represent a global distribution of stations in North America, the Southern Hemisphere, and in Europe.

4.1. SLR Station Analysis

4.1.1. Herstmonceux

[25] Herstmonceux, in southern England, has a climate that is influenced mainly by its close proximity to water resulting in the weather being normally damp and subject to frequent changes. Information from the UK Climate Research Unit (CRU) show that temperature variability for the Central England Time series (CET) is greatest during the winter months compared to other seasons [*Parker et al.*, 1992]. This trend is consistent with our gradient results at Herstmonceux. The statistics in Table 6 show that the standard deviation of the NS and EW gradient delays increase by approximately 10% from summer to winter for both daytime and nighttime values. These seasonal gradient fluctuations are more clearly seen in Figure 3 which shows NS (Figure 3a) and EW (Figure 3b) contributions for both the AIRS and NCEP results during 2004. It is interesting to note that the NS gradients can change by up to 50 mm within a few days during the winter months. As far as diurnal trends are concerned, the NS and EW gradient delays were both smaller during the nighttime observations. The 2-year mean and standard deviation (Table 4) of the NS gradient delay was −3.8 ± 11.3 mm while the EW gradient delay was significantly smaller at −0.2 ± 6.8 mm.

4.1.2. Monument Peak

[26] Monument Peak is situated in the Laguna mountains in California at an altitude of 1800 m, with the Pacific Ocean lying approximately 100 km to the west. The 2-year mean and standard deviation (Table 4) are larger in the EW direction (3.0 ± 9.4 mm) than the NS (−1.3 ± 8.0 mm). We see larger NS and EW gradients during the summer months from April to October with maximum delays reaching up to 30 mm in the NS and 20 mm in the EW direction. The seasonal statistics in Table 6 show that the EW gradients have a preferred positive direction during the summer, indicating the existence of a predominant three-dimensional

Table 3. AIRS and NCEP Horizontal Refractivity Gradients, Expressed as the Delay at 10° Elevation for 2004 and 2005[a]

		2004				2005			
		NS Gradient		EW Gradient		NS Gradient		EW Gradient	
Station	Method	Mean mm	Std mm	Mean mm	Std mm	Mean mm	Std mm	Mean mm	Std mm
Herstmonceux	ART	−4.2	12.0	−0.3	6.6	−3.5	10.7	−0.2	6.8
	NRT	−4.9	10.2	−0.8	5.4	−3.5	8.9	−0.6	5.4
Yarragadee	ART	−3.0	8.1	4.6	9.2	−1.6	7.4	3.5	7.7
	NRT	−3.9	5.6	1.7	3.9	−3.3	5.7	2.2	4.5

[a]ART, AIRS ray tracing; NRT, NCEP ray tracing.

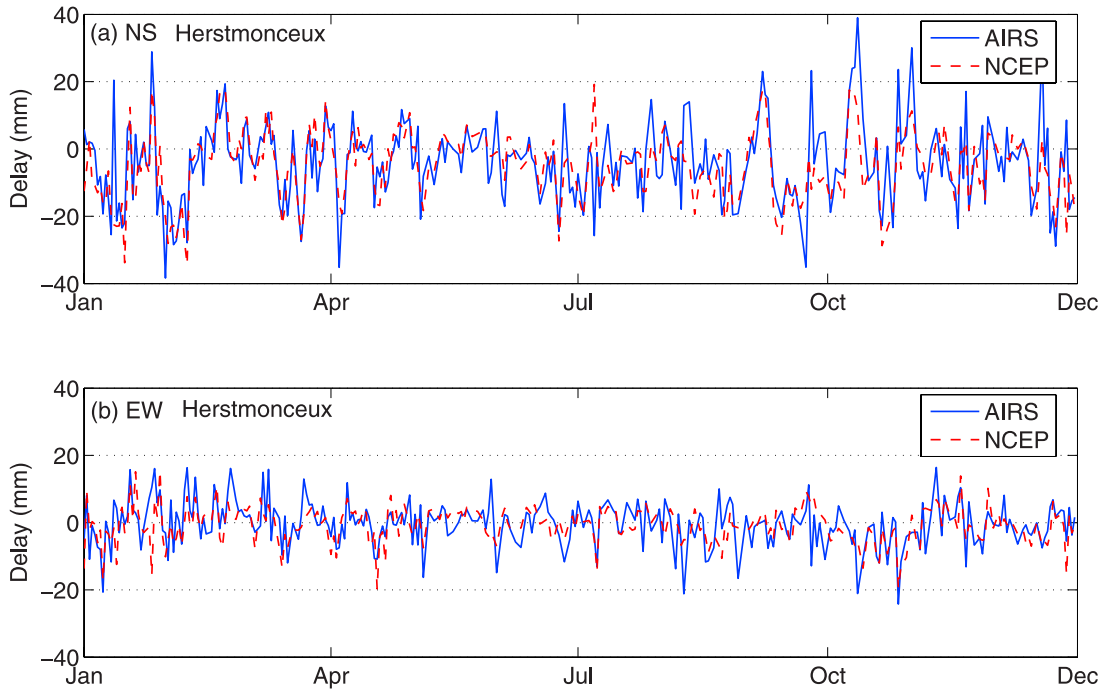

Figure 3. (a) North-south (0° azimuth) and (b) east-west (90° azimuth) gradient delays at 10° elevation for Herstmonceux during 2004 computed using ART and NRT.

structure in the refractivity profiles, most probably as a result of the land-ocean interactions around that particular area.

[27] If we look at the different contributions from pressure and temperature to the gradient delay in Table 5, we find that the absolute magnitude of the pressure gradients are larger during February and August and in both the NS and EW directions. However, it is evident from Figure 5 (bottom right panel) that there are large temperature gradients near the surface during August in the EW direction that can be attributed to larger land-ocean temperature differences during the warmer summer months. It is also interesting to note that the mean temperature gradients change direction above 2 km, resulting in some cancelation and the corresponding mean delay being smaller (0.3 mm) than expected.

[28] Monument Peak's location in a mountainous region at 1800 m above sea level could explain why we see larger

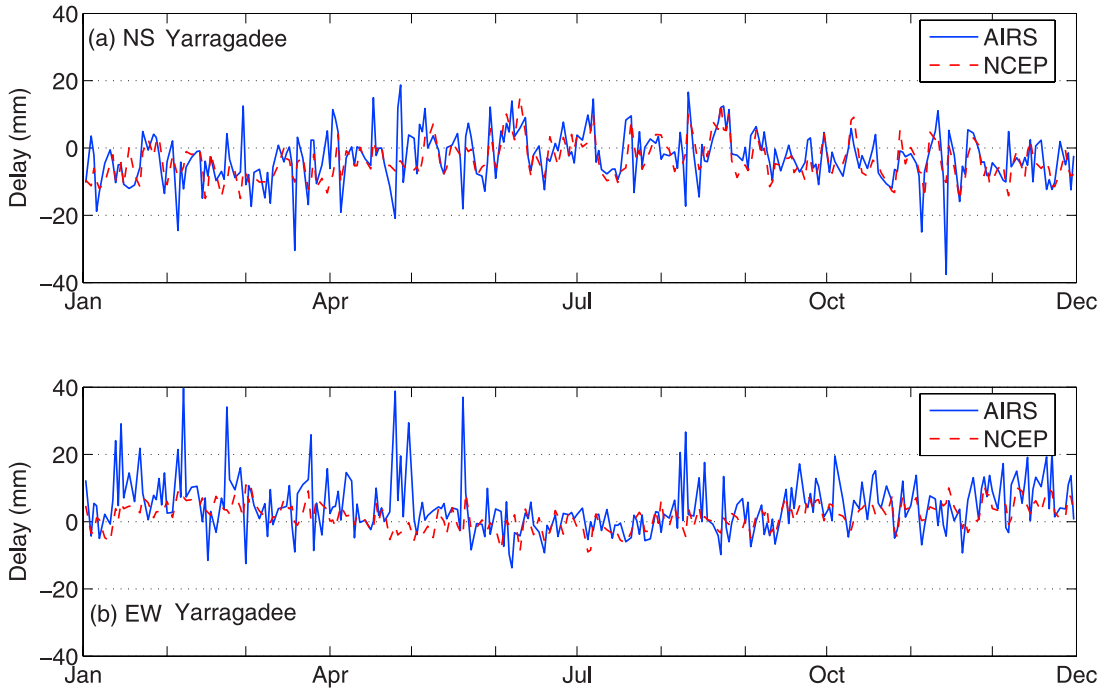

Figure 4. Same as Figure 3 except results are for Yarragadee.

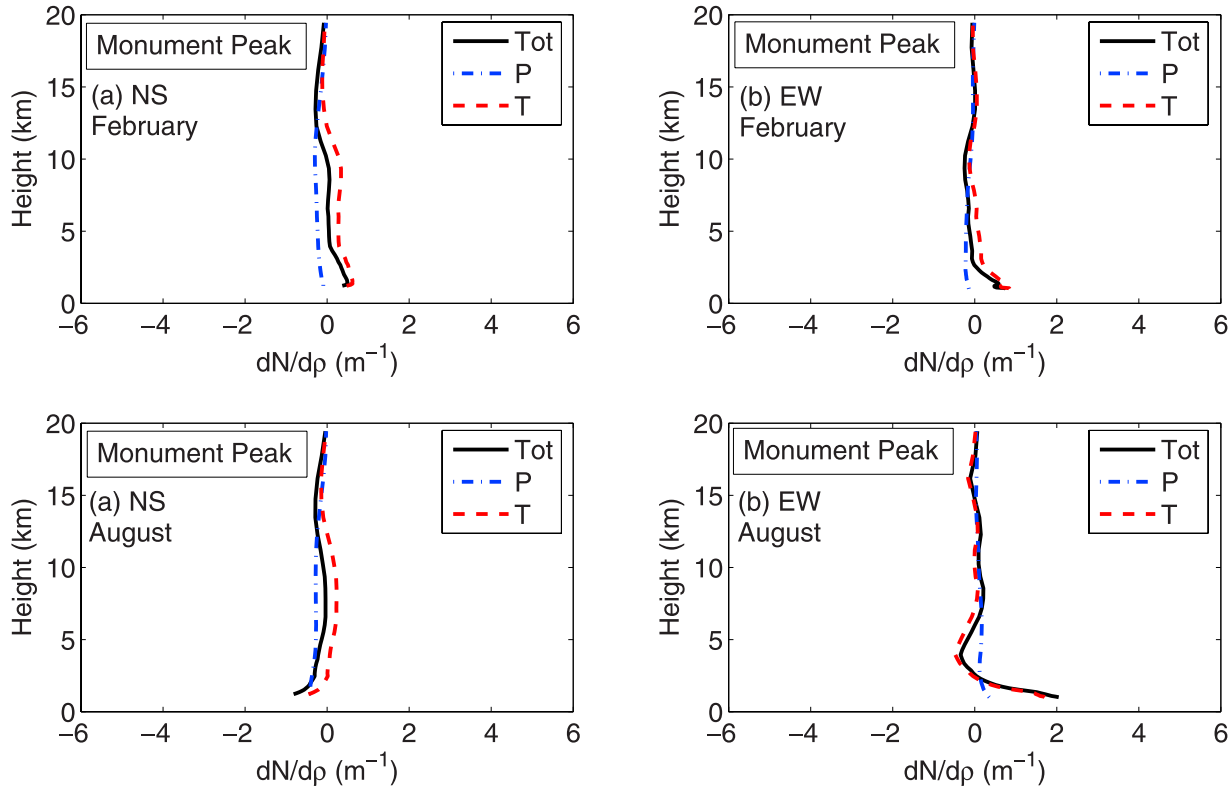

Figure 5. (a) NS and (b) EW mean gradient profiles at zenith showing the total delay and separate contributions from pressure and temperature gradients at Monument Peak during February and August 2004.

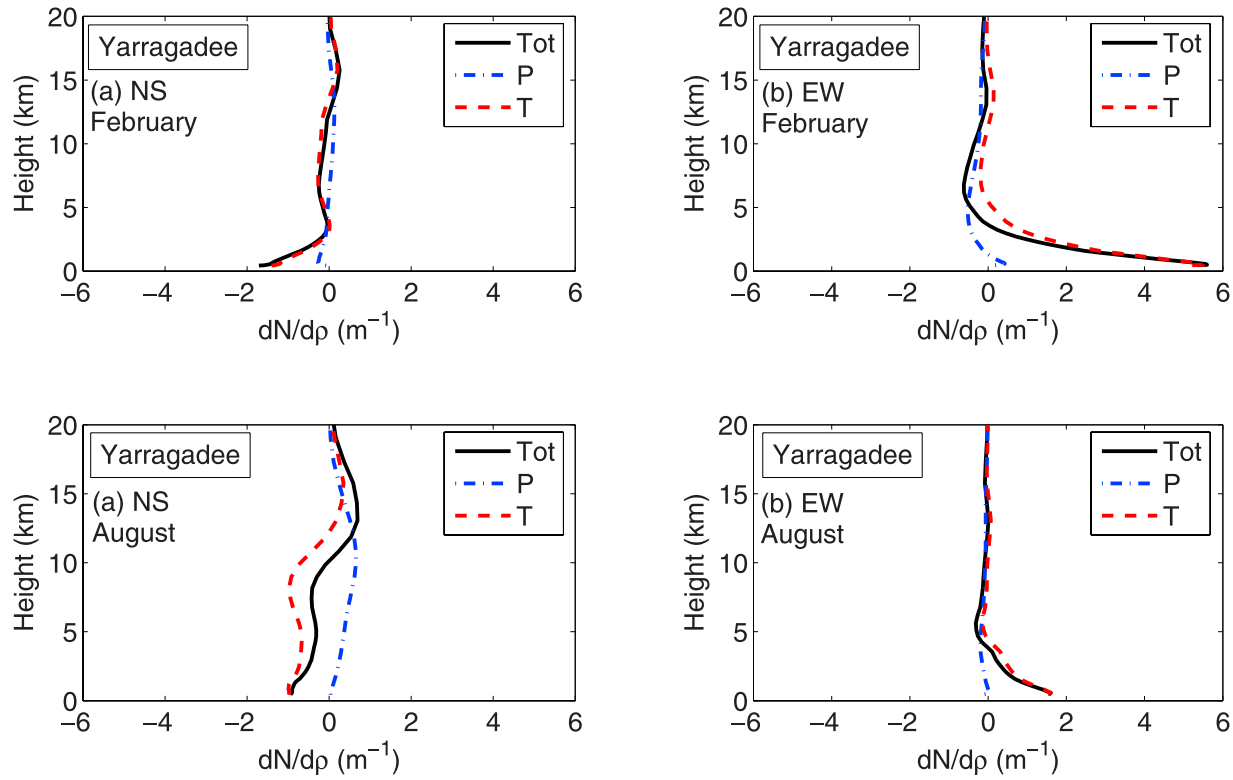

Figure 6. Same as Figure 5, except results are for Yarragadee.

Table 4. AIRS and NCEP Horizontal Refractivity Gradients, Expressed as the Delay at 10° Elevation for 10 ILRS Tracking Stations[a]

Station	Method	NS Gradient Mean mm	NS Gradient RMS mm	EW Gradient Mean Mm	EW Gradient RMS mm
Herstmonceux	ART	−3.8	11.3	−0.2	6.8
	NRT	−4.1	9.5	−0.7	5.4
Graz	ART	−3.6	8.9	1.5	5.5
	NRT	−1.3	6.5	0.3	4.3
Zimmerwald	ART	−4.1	9.1	3.8	6.5
	NRT	−0.8	7.6	0.2	3.3
Matera	ART	−2.1	8.1	1.8	6.4
	NRT	−0.5	4.5	−0.4	4.7
Greenbelt	ART	−1.4	8.4	−1.3	7.5
	NRT	−1.9	5.9	1.0	5.6
Monument Peak	ART	−1.3	8.0	3.0	9.4
	NRT	−0.4	3.0	1.1	2.9
McDonald	ART	0.6	7.0	−2.7	6.0
	NRT	−0.2	3.6	−1.0	3.1
Hartebeesthoek	ART	0.5	5.8	−0.8	5.0
	NRT	2.1	2.2	−1.0	2.0
Yarragadee	ART	−2.2	7.6	4.1	8.0
	NRT	−3.6	5.7	2.0	4.2
Mt. Stromlo	ART	1.9	8.2	1.9	7.3
	NRT	1.0	5.8	−0.1	4.5

[a]Statistics are for 2 years of data during 2004 and 2005. ART, AIRS ray tracing; NRT, NCEP ray tracing.

pressure gradients due to possible deviations in the atmosphere from hydrostatic equilibrium and the effects of vertically trapped waves as discussed by *Hauser* [1991]. We can imagine that the mountains "distort" the pressure profiles around the station, resulting in the larger horizontal pressure gradients. Another possible explanation for the larger pressure gradients could be that horizontal temperature fluctuations in the boundary layer (0–1800 m) are essentially eliminated when calculating the total delay.

4.1.3. Yarragadee

[29] Yarragadee is situated on the south-western coast of Australia and is a very important station in the ILRS network since it produces a very large number of observations and is one of only four operational stations in the Southern Hemisphere. The Indian Ocean lies 50 km to the west of the station, and as a result, we should expect the ocean to have a significant influence on our results. Average summer temperatures in this region range from 28° to 32°C with fluctuations from 20° to 38°C (Australian Climate Bureau) during the summer resulting in large horizontal temperature gradients from land to the cooler ocean. In fact, from our results in Table 6, we find that the largest gradients occur in the EW direction during the summer daytime, with positive mean delays and standard deviation of 11.4 ± 10.9 mm, as compared with values of 4.6 ± 9.2 mm during the winter. The EW gradients have a definite preferred positive direction, indicating that the gradients point eastward, i.e., from cooler values over the ocean in the west, toward warmer air over land in the east. The NS gradients are also significant during the summer months with delays of −6.2 ± 10.1 mm. The gradient delay values for both NS and EW components decrease significantly during the nighttime observations (see Table 6). This can be attributed to the fact that, during the night, the air over land cools down a lot quicker than air over water, and as a result, land-ocean temperature differences decrease, resulting in smaller delay values. The 2-year mean and standard deviations are −2.2 ± 7.6 mm in the NS and 4.1 ± 8.0 mm in the EW direction.

[30] The presence of large EW surface temperature gradients during February can be clearly seen in the temperature gradient profile in Figure 6 (top right panel) when compared to the mean profiles during August (bottom right panel). The corresponding delays for the pressure and temperature contribution for August are similar (Table 5), but during the summer month we see a significantly larger mean and standard deviation for the temperature component.

4.1.4. Zimmerwald

[31] Zimmerwald is stationed near Bern, Switzerland, and although the climate is temperate throughout the year with temperatures not too hot or cold, the varying topography (altitudinal spread of more than 4000 m) is one of the main factors that affect the climate in different regions of the country. If we look at the 2-year seasonal and diurnal variations (Table 6), we see a relatively large, positive mean EW gradient of 4.4 ± 5.9 mm. For the NS component, there

Table 5. Corresponding Delays From Figures 5 and 6 Showing Separate Contributions From Temperature and Pressure Toward the Gradient Delay[a]

Station	Contribution	NS Gradient Mean mm	NS Gradient Std mm	EW Gradient Mean mm	EW Gradient Std mm
Monument Peak					
February	Total	−0.2	0.8	−0.4	0.8
	Pressure	−1.8	1.7	−1.1	1.4
	Temperature	1.6	1.4	0.6	1.0
August	Total	−2.1	1.5	1.5	0.9
	Pressure	−2.3	1.6	1.2	3.0
	Temperature	0.2	1.1	0.3	2.7
Yarragadee					
February	Total	−1.1	1.1	1.4	1.3
	Pressure	0.1	1.9	−2.4	2.6
	Temperature	−1.6	2.2	4.2	4.0
August	Total	0.1	1.1	0.3	0.6
	Pressure	3.5	1.5	−0.8	1.4
	Temperature	−3.4	1.1	1.2	1.8

[a]Statistics are for February and August 2004 at Monument Peak and Yarragadee.

Table 6. Seasonal and Diurnal Horizontal Gradient Delay Variations at 10° Elevation for 2 Years During 2004 and 2005, Using ART

Station	Season	Time	NS Gradient Mean mm	NS Gradient Std mm	EW Gradient Mean mm	EW Gradient Std mm
Yarragadee	Summer	day	−6.2	10.1	11.4	10.9
		night	−4.0	5.1	5.7	4.9
	Winter	day	−2.6	9.1	4.6	9.2
		night	−0.1	6.2	1.0	6.0
Herstmonceux	Summer	day	−5.4	11.2	−0.6	6.3
		night	−2.7	9.5	0.5	5.9
	Winter	day	−3.9	12.5	−0.4	7.0
		night	−3.0	11.0	−0.2	7.3
Monument Peak	Summer	day	−2.5	10.3	5.8	11.7
		night	−4.4	4.6	5.1	5.5
	Winter	day	−0.4	6.6	1.1	7.7
		night	−0.5	5.2	2.3	6.1
Zimmerwald	Summer	day	−2.9	7.8	4.4	5.9
		night	−8.3	8.0	3.3	5.2
	Winter	day	−3.4	9.3	3.9	7.1
		night	−5.1	10.5	3.1	6.3

are larger variations during the winter for both day and night values with standard deviations increasing from 7.8 to 9.3 mm during the day from summer to winter and from 8.0 to 10.5 mm during the night from summer to winter. The EW gradients are constant throughout the year with similar mean and standard deviation values during the summer and winter. It is interesting to note here that the NS standard deviations during the summer nights are comparable, if not larger than the daytime values. At all other stations the nighttime gradients appeared to be smaller with less variations.

4.2. Hydrostatic and Nonhydrostatic Contributions

[32] Of the four space geodetic techniques mentioned (SLR, VLBI, GPS, Satellite Altimetry), SLR optical frequencies are the most insensitive to the two most unpredictable components of the atmospheric delay, the ionosphere and water vapor distribution. Laser wavelengths in the visible and ultraviolet are far from strong water absorption lines in the spectral regions between 0.7 and 1.0 μm, thus the hydrostatic (dry) component of the atmosphere is the main contributor to the propagation error in SLR. The hydrostatic component of the delay arises from the dry gases (oxygen, nitrogen, and other trace gases) and the nondipole component of water refractivity in the atmosphere. The nonhydrostatic (wet) delay includes only the dipole component of water vapor refractivity and varies much more in time and space than the hydrostatic delay.

[33] Measurements made in the zenith direction induce delays (excluding horizontal gradients) of approximately 2.5 m for the dry and less than 10 mm for the wet component at optical wavelengths. In comparison, the zenith wet delay can be as large as 30 cm for microwave systems. *Chen and Herring* [1997] found wet gradient delays of up to 20 mm at 10° elevation, and there have been other studies using water vapor radiometry (WVR) data that have found gradients with similar magnitudes [*Davis et al.*, 1993]. We should, however, expect the wet contribution from the horizontal gradient delay to be very small at optical wavelengths, and our results show this. We looked at results for Greenbelt, Maryland which has relatively high humidities with monthly averages ranging from 70 to 80% during the summer months. We calculated wet delays with mean and standard deviation of 0.01 ± 0.1 mm from May to September 2004 at Greenbelt. The maximum wet gradient delay we observed was approximately 0.3 mm on 22 August 2004. We can therefore conclude that wet gradient delays can be ignored in estimating the total gradient delay for SLR purposes.

4.3. AIRS Error Propagation

[34] Since the gradient delays are relatively small (centimeter level or less at 10°) when compared to the total delay (up to 14 m at 10°), we need to establish whether the gradient delay results estimated from AIRS data are from actual day-to-day gradient variations or from possible errors in the data. We accomplish this by propagating AIRS uncertainties into our gradient delay calculations. This is done by generating a second set of simulated AIRS data by adding in Gaussian white noise to the temperature profiles. We use AIRS uncertainties provided by recent validation results in order to generate the noisy data. The validation results apply to latitudes from 50°S to 50°N, and AIRS retrieved temperature profiles are compared to data from the European Center for Medium Range Weather Forecasting (ECMWF) and dedicated radiosondes. RMS differences between AIRS and ECMWF were found to be approximately 1.3 K in the boundary layer and less than 1 K in the troposphere. The calculations were made over 1-km-thick layers in the troposphere. Radiosonde comparisons showed uncertainties of 1 K in the troposphere. AIRS temperature profiles above 50 mb are more difficult to validate, but uncertainties of around 2 K were estimated. RMS differences between AIRS water vapor profiles and radiosondes vary with height from ~30% at the surface to ~12% in the troposphere. We do not include the water vapor uncertainties in our simulated data, since the contribution of the wet gradient component is very small (as mentioned in the previous section), and the corresponding uncertainty would be negligible.

[35] In order to generate the AIRS simulated temperature data, we use the RMS values for temperature as described above at the appropriate levels. We use an RMS of 1.3 K for the first 2 km in the atmosphere, 1 K in the troposphere until 300 mb, and 2 K above 300 mb. Uncertainties above 300 mb do not have a significant effect on the total error, since the gradients become very small at this height. In order to make comparisons, we calculate the difference between gradient delays using the original (O) and simulated (S) data at 10° elevation and at 8 azimuths from 0° to 315° at Herstmonceux and Yarragadee during February and August 2004.

[36] Top panels in Figure 7 show the mean total gradient delay (i.e., NS + EW components combined) results from ray tracing at eight selected azimuths and for two elevation angles of 10° and 20°. The gradient variations are sinusoidal with respect to azimuth, and so we use a least squares fit for amplitude, phase, and bias of a sinusoid. The average EW gradient delay component (90° and 270° azimuth) is less than the NS component (0° and 180° azimuth) at Herstmonceux; however, the opposite is true at Yarragadee, and this is a result of strong EW gradients in this area. At 20° elevation, the delays decrease considerably and are approximately one third of the delay at 10° elevation for all azimuths at both stations. Theoretically, using the MTT gradient-mapping function [*Chen and Herring*, 1997], the gradient delay amplitudes will vary as $\sim 1/\sin(e)^2$. As a result the delay should decrease by a factor of four from 10° to 20° elevation. However, the gradient-mapping function assumes the gradients to have the same direction at all levels, resulting in a larger scaling factor when compared to the ray-tracing results that realistically estimate the gradient directions at all altitudes. The bottom panels in Figure 7 show the corresponding standard deviations at each azimuth and for the two elevation angles. Maximum standard deviations occur in the NS and EW directions.

[37] Figure 8 shows mean values (circles) and error bars of the original (O) minus the simulated (S) gradient delays for February and August 2004 at Herstmonceux (left panels) and Yarragadee (right panels). Both stations had mean values at the submillimeter level, with maximum standard deviations of approximately 5 mm for both months used in the analysis. The standard deviations in Figure 7 are a result of a combination of actual day-to-day changes in the gradients and standard errors in the data used. For example,

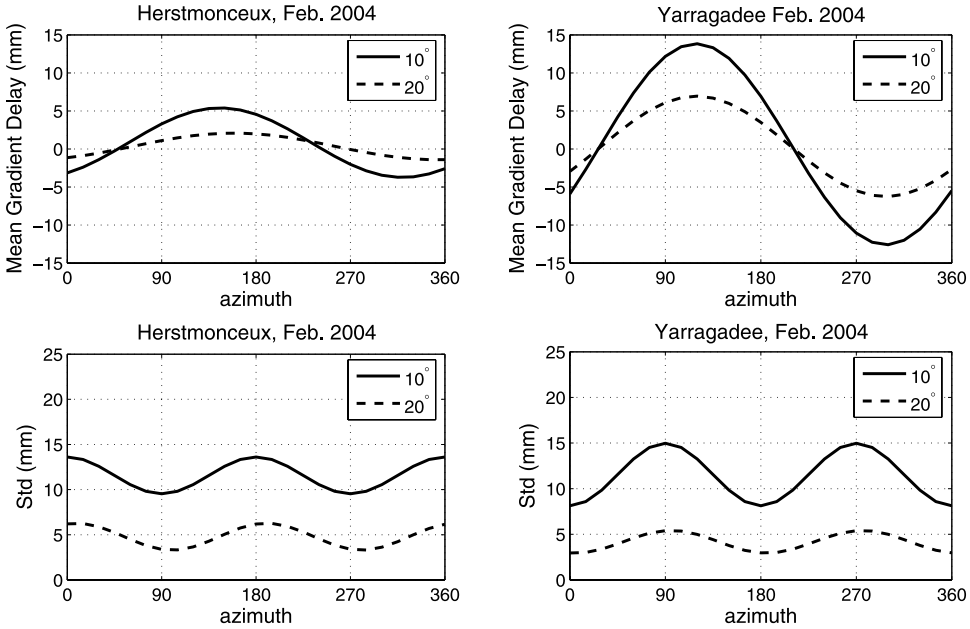

Figure 7. Mean total gradient delay values (NS + EW components) and corresponding standard deviations for Herstmonceux (left panels) and Yarragadee (right panels) during February 2004 at eight different azimuths and two elevation angles of 10° and 20°.

at 10° elevation and 0° azimuth at Herstmonceux during February, the mean gradient delay calculated using the original (O) data was 4.2 mm, with a standard deviation of 13.6 mm and a corresponding standard RMS error of 4 mm. As a result, the actual day-to-day gradient variations are approximately $\sqrt{13.6^2 - 4^2} = 13$ mm. Similarly, by looking at all azimuths at Herstmonceux during February 2004, we can conclude that actual day-to-day gradient RMS variations range from 9 to 13 mm at 10° elevation, with the variations in standard data errors at the 2- to 5-mm level. Performing a similar analysis at Yarragadee results in day-to-day RMS variations of between 7 and 14 mm, with RMS errors in the data again ranging from 2 to 5 mm during February 2004. The standard errors during August 2004 are of similar magnitude to the February results. We can therefore conclude that AIRS data is accurate enough to

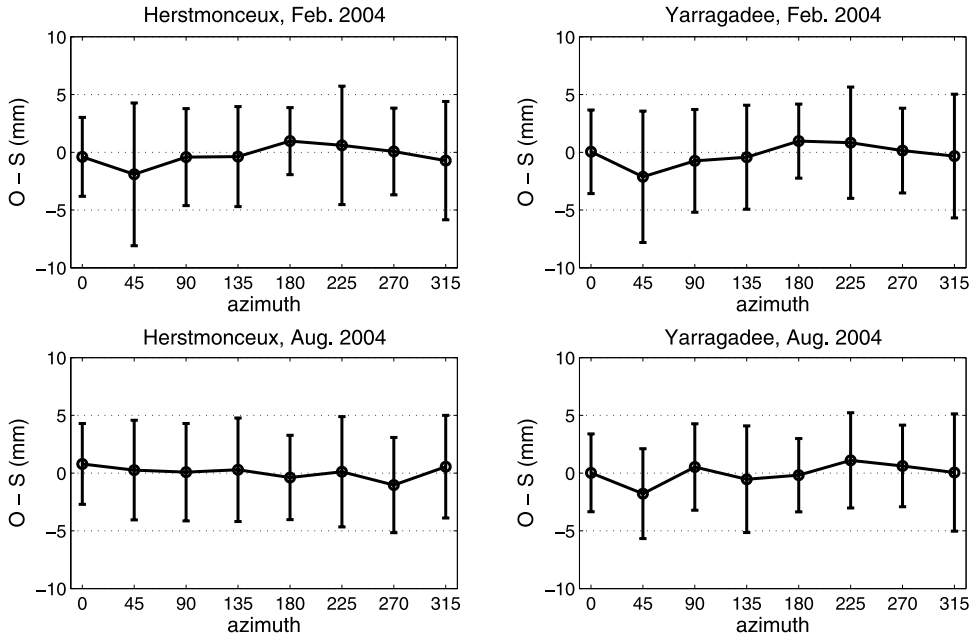

Figure 8. Mean (circles) and standard deviations (error bars) of the difference between original (O) and simulated (S) gradient delays using AIRS data for Herstmonceux (left panels) and Yarragadee (right panels) during February (top panels) and August (bottom panels) 2004, at eight different azimuths and an elevation angle of 10°.

estimate changes in horizontal refractivity gradients at the centimeter level.

5. Global Results

[38] In order to get a broad overview of what type of gradients to expect globally, we calculate the gradient delays by ray tracing through AIRS level 3 data. The AIRS level 3 gridded data is derived from the level 2 product using quality control factors that determine which profiles are of good quality. We use the monthly product which is simply the arithmetic mean of all data obtained during that month and combined into each grid box. The data is divided up into an ascending (south to north) and descending (north to south) portion of the AIRS orbit, corresponding to daytime and nighttime, respectively. The daily product contains empty spaces between the satellite paths with no data coverage, but with the monthly product, we should expect complete global coverage with almost no missing data. The data are binned into $1^\circ \times 1^\circ$ grid cells.

[39] As far as validation is concerned, the level 3 data has been validated for nonpolar latitudes between 50°N and 50°S. All the products we used have been validated over both land and ocean, except for the surface temperatures that have only been validated over ocean. None of the products have been validated over ice or snow. We perform the ray tracing at 10° elevation at every cell within the gridded data (180×360) in the NS (0° azimuth) and EW (90° azimuth) directions during January and August 2004 and for a total of 64,800 ray traces.

[40] Our results in Figure 9 show strong correlations between surface temperature changes (top panels) and the gradient delay results, particularly in the NS direction. There are very strong NS gradient delays of up to 40 mm in absolute magnitude in the midlatitude regions around 45°. In Figure 10 we notice that there is a larger variability during the Northern Hemisphere winter with standard deviations at the 25-mm level over north eastern USA and parts of Europe. Our results at Herstmonceux and Zimmerwald confirm the larger variability during winter (see Table 6). Other areas showing consistently large NS gradients (independent of time period chosen) are along the Andes mountains in South America, the Tibetan Plateau, the Northern Atlantic [North Atlantic Oscillation (NAO)], and over the Northern Pacific (Aleutian low pressure system). The global average NS gradient delay is at the 5- to 10-mm level.

[41] Large EW gradients also occur in the midlatitude regions, with higher variability during the Northern Hemisphere winter. Areas with large positive EW gradient delays in January occurred on the west coast of Australia near Yarragadee, along the Namibian coast in South West Africa where the cold Benguela current meets the hot Namib desert, and along the entire Andes Mountain Range in South America. The Northern Hemisphere experienced larger EW variations during January, particularly over Northern America and Eastern Asia. During August, we notice positive EW gradient delays larger than 10 mm on the US west coast near Monument Peak and delays at the 5-mm level over Europe. On a whole, the EW gradient delays are smaller than the NS, with global means at the 50-mm level. We notice an overall trend where the EW gradients have consistently higher values in the same direction along the coast during the summer due to large land-ocean temperature differences, while they become more variable during the winter. It is also interesting to note from our results that Arequipa SLR station, situated on the west coast of South America in Chile, would experience consistently large NS and EW gradients throughout the year.

[42] We see very similar patterns between our results in January and corresponding global gradient results from the work of *MacMillan and Ma* [1997], who used atmospheric profiles from the Data Assimilation Office at NASA Goddard during January 1990 at a resolution of 200 km. Gradients of similar magnitudes were observed; however, the AIRS results had a lot more variation, due to the much higher resolution (~50 km). *Chen and Herring* [1997] estimated global gradient delays by using NCEP data, and the results showed similar gradient trends and magnitudes when compared with ours, particularly in the NS direction for both months used in the analysis. However, the AIRS gradient standard deviations are again much larger. For example, we find large bands of NS standard deviations ranging from 20 to 30 mm at latitudes of 50°N and 50°S in Figure 10, while corresponding standard deviations calculated from the work of *Chen and Herring* [1997] for the same month and latitudes ranged from 5 to 10 mm. This is most likely due to the much lower spatial resolution of the NCEP data (~250 km) when compared to AIRS data (~50 km).

6. NCEP Gradient Comparisons With AIRS

[43] In Figure 3 we see similar trends between the AIRS and NCEP gradient results for both NS and EW components at Herstmonceux. The NS gradient patterns are also similar at Yarragadee (Figure 4); however, in the EW direction, NCEP does not capture the larger gradients as seen by AIRS. We think this is primarily due to the low spatial resolution of the NCEP data (250 km) when compared to AIRS (50 km). Even though the AIRS and NCEP gradients have the same direction for most observations, it appears that the NCEP temperature fields get averaged out over a larger area, resulting in much smaller gradient delays, particularly in the EW direction for most stations. Our results in Table 4 also indicate that AIRS has much larger standard deviations than NCEP at all stations and for both components. As a result, the use of NCEP data may be inadequate in estimating gradient delays, as the data is insensitive to small-scale (<50 km) gradient fluctuations that contribute significantly to the total delay for SLR observations.

7. Effects of Ray Tracing on SLR Solution Residuals

7.1. Observation Residuals

[44] We now look at the impact of using ART and NRT on the analysis of a set of real SLR data for geodetic satellites LAGEOS 1 and 2 during 2004 and 2005. The data we used from the SLR stations as input to the ray-tracing program are station number, day of year, time of day, true elevation and azimuth of the outgoing ray, wavelength of the laser, surface pressure, surface temperature, and relative humidity at the surface. There are approximately 1500 observations per weekly arc for the entire network of SLR stations. From this we select data for the 10 stations chosen in our analysis

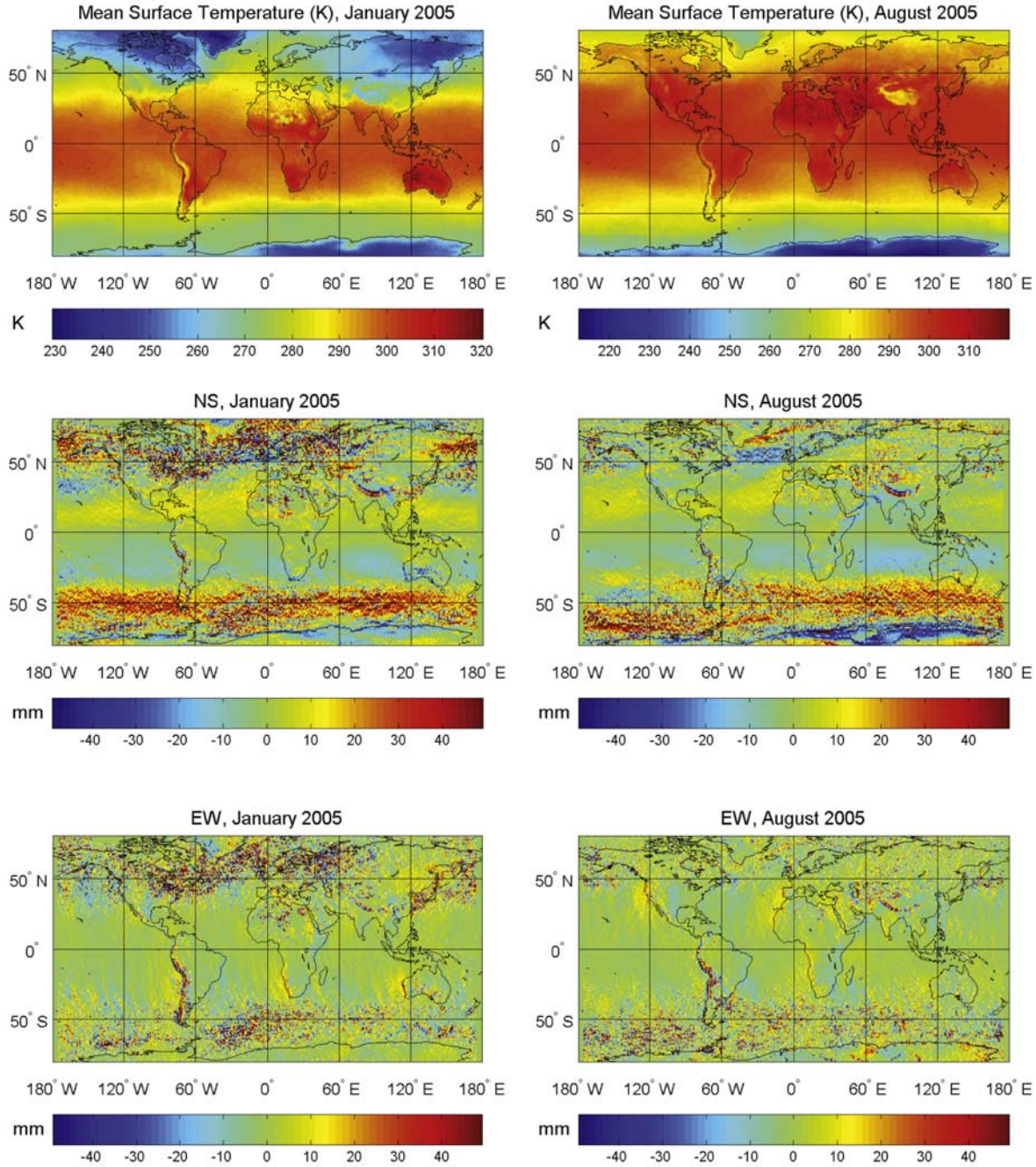

Figure 9. Mean AIRS surface temperatures (top panels) and gradient delays at 10° elevation for NS (middle panels) and EW (bottom panels) components computed during January (left panels) and August (right panels) 2005.

and the availability of AIRS data for any particular day. We do this since it sometimes occurs that an AIRS granule will not cover a large enough area surrounding the station to perform the ray tracing. NCEP data was available for all observations, but for comparison purposes, we only used NCEP observations that were concurrent with AIRS.

[45] Our primary goal is to generate more accurate SLR data that can be used in applications such as improving the accuracy of the origin and scale of the International Terrestrial Reference Frame (ITRF) [*Altamimi et al.*, 2002] and to improve geodetic models that are required in Precise Orbit Determination (POD) [*Luthcke et al.*, 2003]. We use the GEODYN orbit determination and geodetic parameter estimation software for the POD analysis [*Pavlis et al.*, 1998], and this requires accurate models of tides, gravity, and reference frames. We aim to improve the accuracy of the refraction corrections by using ray tracing with global meteorology data in order to minimize the SLR solution residuals for each observation. The residuals are the actual observed ranges to the satellite minus the calculated ranges ($R = O - C$). The residuals at present are typically between ±30 mm and have a standard deviation of approximately

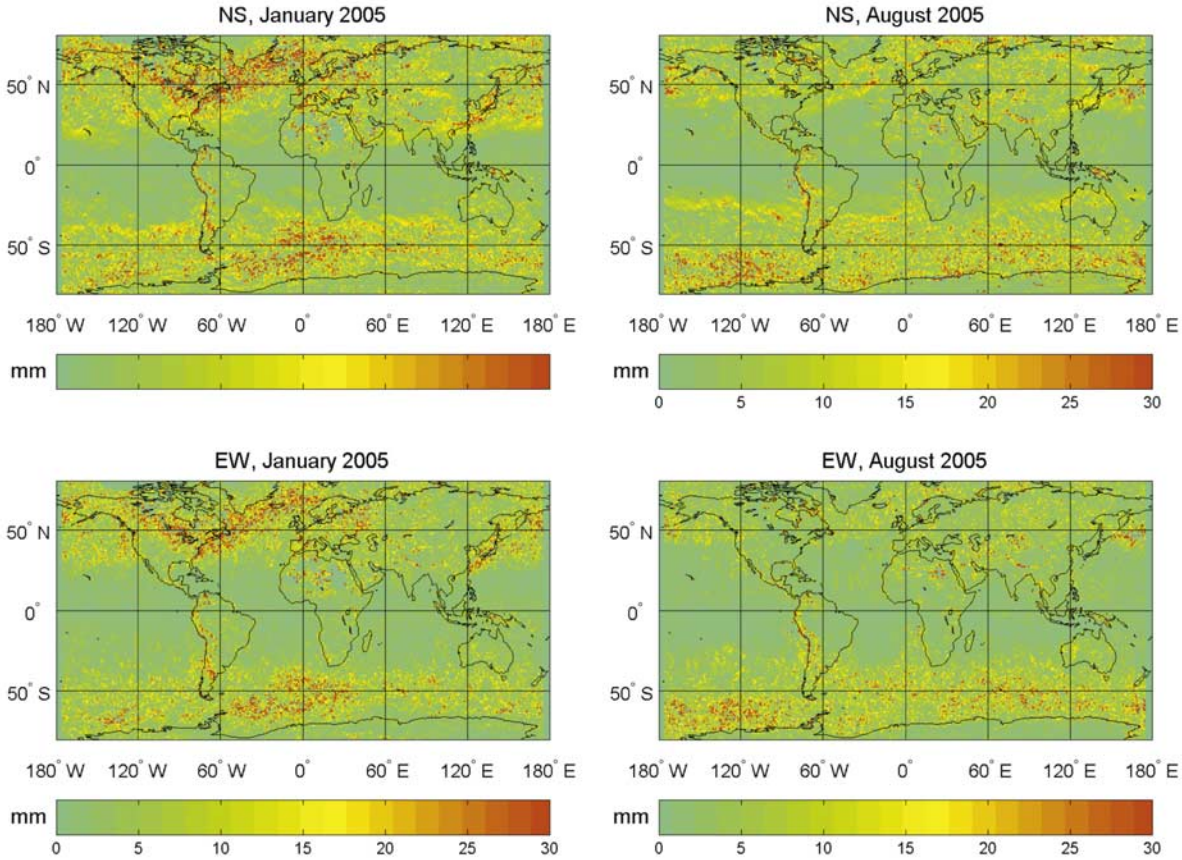

Figure 10. Standard deviation of AIRS gradient delays at 10° elevation for NS (top panels) and EW (bottom panels) components computed during January (left panels) and August (right panels) 2005.

10 mm. The observed ranges include all atmospheric effects and must first be preprocessed in order to remove errors such as model biases. The calculated or geometric ranges are computed using an assumed math model with an estimate of the desired parameters calculated using a least squares method. Various effects from the atmosphere, tides, ocean loading, and gravity must first be removed before meaningful results are to be obtained. The atmospheric effects are currently computed using the M-P atmospheric delay model [*Mendes and Pavlis*, 2004]. Our goal is to replace the model with full ray-tracing results using input data from AIRS and from numerical weather models such as NCEP. In this way, the total atmospheric delay, including the gradient corrections, can be evaluated using near real-time atmospheric conditions in order to obtain the most accurate corrections possible.

7.2. Data Preprocessing

7.2.1. Temporal Interpolation

[46] Before the ray tracing can be performed, the atmospheric profiles have to be temporally interpolated in order to coincide with the observation time at the station. We use the NCEP analysis files that are available every 6 h, combined with a simple linear temporal interpolation scheme, to compute new atmospheric profiles at the station observation times. Temporally interpolating the AIRS data can be more complex since there is occasionally only one AIRS granule available for any particular day, resulting in possible time differences of up to 12 h between the AIRS and station observations. We developed a scheme where, if two AIRS granules were available for any given day, we simply used the linear interpolation scheme for the NCEP data. However, if only one AIRS granule was available, we calculated temporal gradients between successive NCEP observations that encompassed the AIRS time of observation and used these gradients to project any AIRS geophysical parameter (i.e., temperature) either forward or backward in time in order to coincide with the station observation time. We found this temporal interpolation scheme for AIRS to be successful and noticed decreases in residual RMS values of a millimeter or less as a result.

7.2.2. Boundary Layer Interpolation

[47] The majority of SLR station surface measurements of temperature, pressure, and relative humidity are made with the MET3 Meteorological Measurement System [*Paros and Yilmaz*, 2002]. The accuracy is ±0.5°C for temperature, ±0.08 mb for pressure, and ±2% for relative humidity. Because of the higher accuracy of the MET3 surface measurements, we replace the equivalent AIRS or NCEP surface observations with them. In order to avoid large discontinuities in the data as a result of this, the MET3 measurements are interpolated into the first 2 km of the atmospheric profiles. This process also eliminates uncertainties in boundary layer temperatures for NCEP and, in particular, AIRS data. For the gradient ray tracing, we do not include the MET3 values since there are no measure-

ments made surrounding the stations needed to compute surface gradients.

7.3. Residual Corrections

[48] We make corrections to the calculated ranges (C) in the following two different ways: (1) We keep the atmospheric correction from the M-P model, but include horizontal gradient corrections, and (2) we replace the M-P model correction with two-dimensional ray-tracing results and include horizontal gradient corrections to get a total correction.

[49] 1. $R_g = O - (C + \Delta\text{trop}_g)$

[50] 2. $R_t = O - (C - \Delta\text{trop}_{mp} + \Delta\text{trop}_{2d} + \Delta\text{trop}_g)$

where R_g and R_t are the gradient-corrected and total-corrected residuals, O are the observed ranges, C are the computed ranges using the M-P model for refraction corrections, Δtrop_g is the ray-tracing gradient correction, Δtrop_{2d} is the atmospheric delay calculated using two-dimensional ray tracing, and Δtrop_{mp} is the atmospheric delay calculated using the M-P delay model.

[51] 1. $R_g = O - (C + \Delta\text{trop}_g)$

[52] 2. $R_t = O - (C - \Delta\text{trop}_{mp} + \Delta\text{trop}_{2d} + \Delta\text{trop}_g)$

where R_g and R_t are the gradient-corrected and total-corrected residuals, O are the observed ranges, C are the computed ranges using the M-P model correction, Δtrop_g is the gradient correction, Δtrop_{2d} is the atmospheric delay calculated using two-dimensional ray tracing, and Δtrop_{mp} is the atmospheric delay calculated using the M-P delay model.

7.4. Results

[53] We analyze the SLR solution results by looking at the bias difference $\Delta\text{Bias}_{g/t}$ and variance percent difference $\Delta\sigma^2_{g/t}$ between the corrected $R_{g/t}$ and the original solution residuals R. The subscript "g" indicates that only the gradient correction was applied, and subscript "t" indicates that the total correction (two-dimensional ray tracing + gradient correction) was applied. The bias difference is simply the difference in the mean values of R and $R_{g/t}$ and is given by

$$\Delta\text{Bias}_{g/t} = |\text{mean}(R)| - |\text{mean}(R_{g/t})| \tag{13}$$

The variance is a measure of the spread or dispersion of a data set, and the variance percent difference between R and $R_{g/t}$ will give an indication of improvement due to the new corrections as follows:

$$\Delta\sigma^2_{g/t} = \frac{\sigma^2(R) - \sigma^2(R_{g/t})}{\sigma^2(R)} \cdot 100 \tag{14}$$

[54] We analyze the new results by using equations (13) and (14). The total number of observations used in the statistics for all stations and for 2 years of data was 47,664. Positive values of equation (13) and, more importantly, equation (14) indicate a smaller bias and variance in the residuals and hence an improvement in our results.

[55] Figure 11a shows bias and variance differences for the gradient-corrected residuals for LAGEOS 1. We see improvements at all stations and for both AIRS and NCEP when including the gradient corrections in the residual analysis. The bias differences are at the submillimeter level for both data sources. The corresponding residual variances show improvements of between 10–15% for AIRS and 5–10% for the NCEP results. Overall, AIRS ray-tracing results had the largest reductions in variance when compared to NCEP for the majority of the stations. This can be attributed to the much higher spatial resolution of the AIRS data, providing the ability to calculate the gradients more accurately and on a much finer scale.

[56] Figure 11b shows bias and variance differences for the total-corrected residuals for LAGEOS 1. Overall, there is a larger improvement in the results when the total correction is applied, and this can be seen as an increase in variance percent difference from Figures 11a to 11b. However, we notice that, for a few stations (for example, GZ, YA, and MS), there is a drop in variance difference of a few percent for AIRS, in other words, a smaller improvement when compared to the gradient-corrected results. We think this could be due to some kind of cancelation effect when adding the gradients to the two-dimensional ray-tracing results or the gradients could be over or under-estimated at these locations. The NCEP results, on the other hand, show larger improvements in variance than AIRS at all stations, with values ranging from 30 to 40% at most stations. However, we see larger NCEP bias differences of up to 5 mm at all stations except MP, even though the corresponding variances are significantly improved. Possible reasons for the large biases could be (1) the low spatial resolution of the data, and (2) that it has been found that the NCEP tropopause temperature is too warm by 3–5 K and too high in pressure by 2–6 mb when compared to radiosonde data [*Randel et al.*, 2000]. Comparisons were made for the period 1979–1997, and these biases were found to be constant in time.

[57] The LAGEOS 2 results in Figure 12 are very similar with respect to levels of improvement for all data sources. We again see significant reductions in variance for the gradient- and total-corrected results and smaller AIRS improvements at GZ, YA, and MS when compared to the gradient-corrected results. The results shown here are very promising in that any improvements in the solution residual results, particularly in variance, will automatically imply improvements in the repeatability of station position coordinates, and hence a more accurate and stable ITRF. This is the next step of our investigation, after the implementation of the new atmospheric delay corrections in the NASA Goddard POD and geodetic data reduction software, GEODYN [*Pavlis et al.*, 1998].

[58] Figure 13 shows what type of seasonal variations to expect when using the total-corrected solution residuals for each weekly arc of data for the LAGEOS 1 results during 2004. The plot shows RMS differences, which will include a combination of bias and variance differences, for four of the most prolific SLR stations in terms of data yield. Once again, positive values indicate an improvement in the estimation of the corrected SLR residuals. Gaps in the data indicate that there were no observations at that particular station for the specified time period. We do not observe any seasonal trends at all the stations, although, during the winter months at Herstmonceux, it appears that the NCEP results have a large number of arcs with negative RMS differences. This is primarily due to large biases in the NCEP correction residuals. Monument Peak, which is

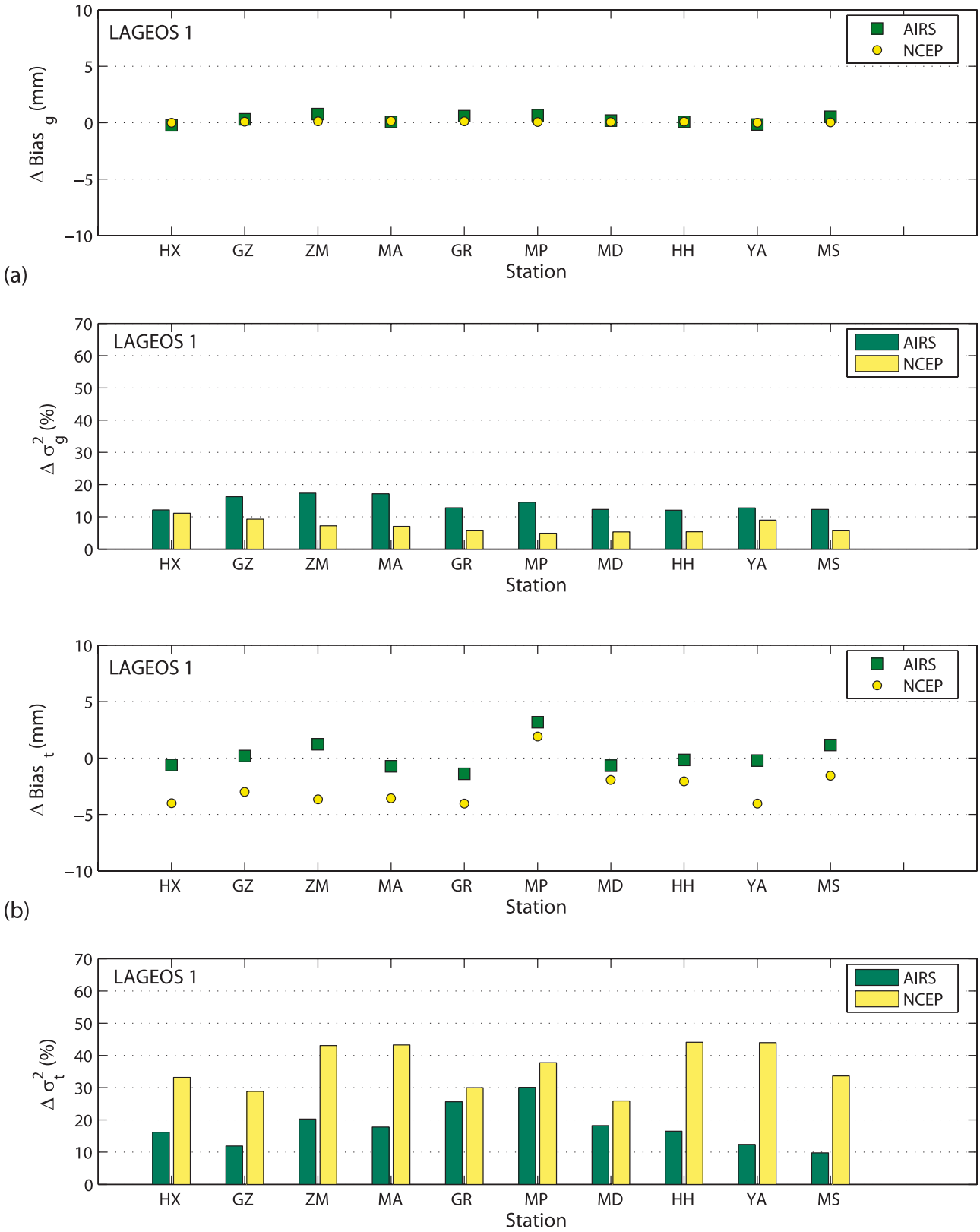

Figure 11. Bias (top) and variance (bottom) differences between (a) the gradient-corrected and (b) the total-corrected solution residuals for LAGEOS 1 for 2 years of data, 2004 and 2005 and for all 10 SLR stations.

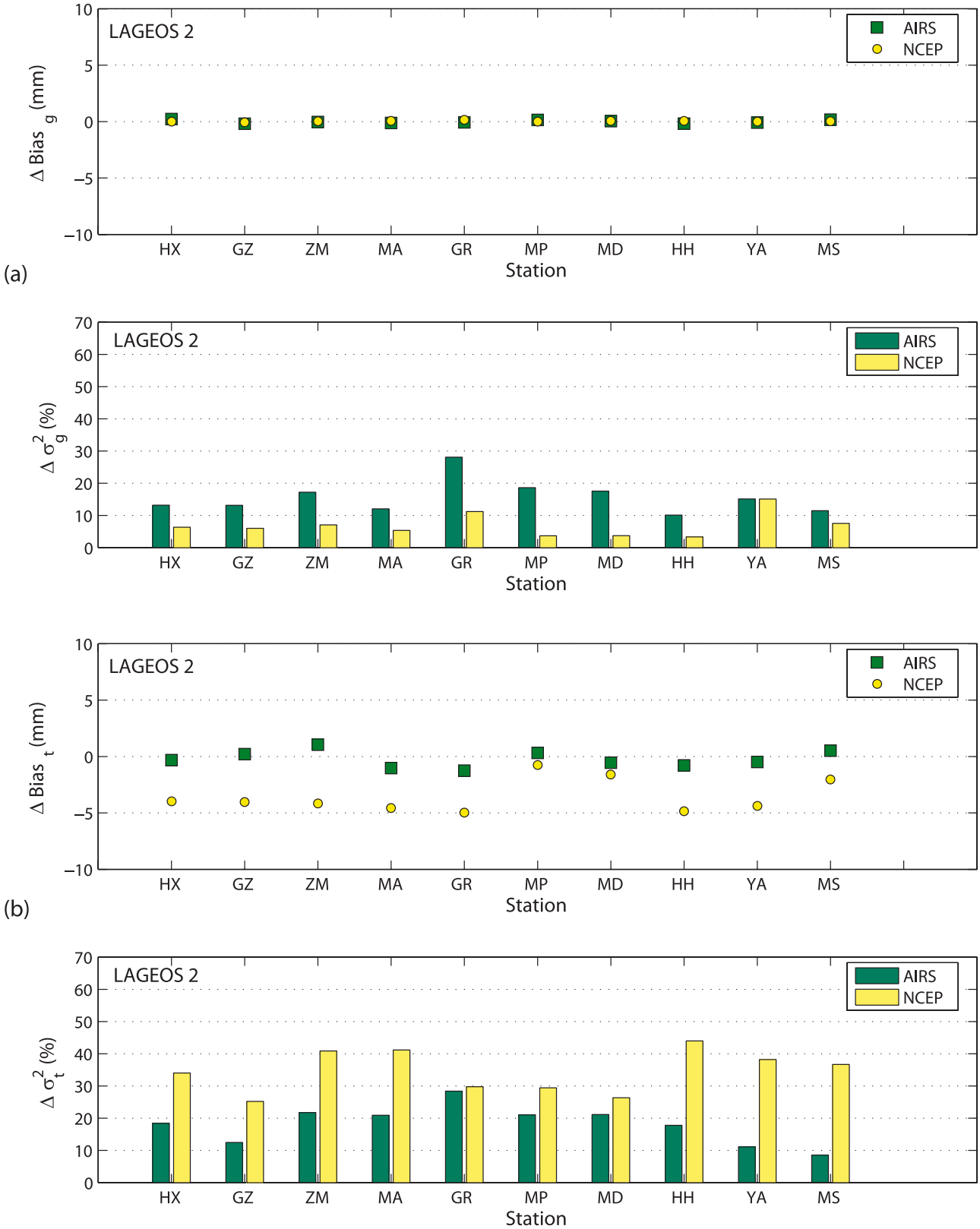

Figure 12. Same as Figure 11, except results are for LAGEOS 2.

situated in a very mountainous region and close to the ocean, shows overall large positive difference in RMS for AIRS and NCEP results. This could be due to the failure of the delay models to account for changes in delay at different azimuths around the station. As a result, the ray-tracing results through the high-resolution three-dimensional grids show large improvements in the variance of the solution residuals. Yarragadee and Zimmerwald show mostly posi-

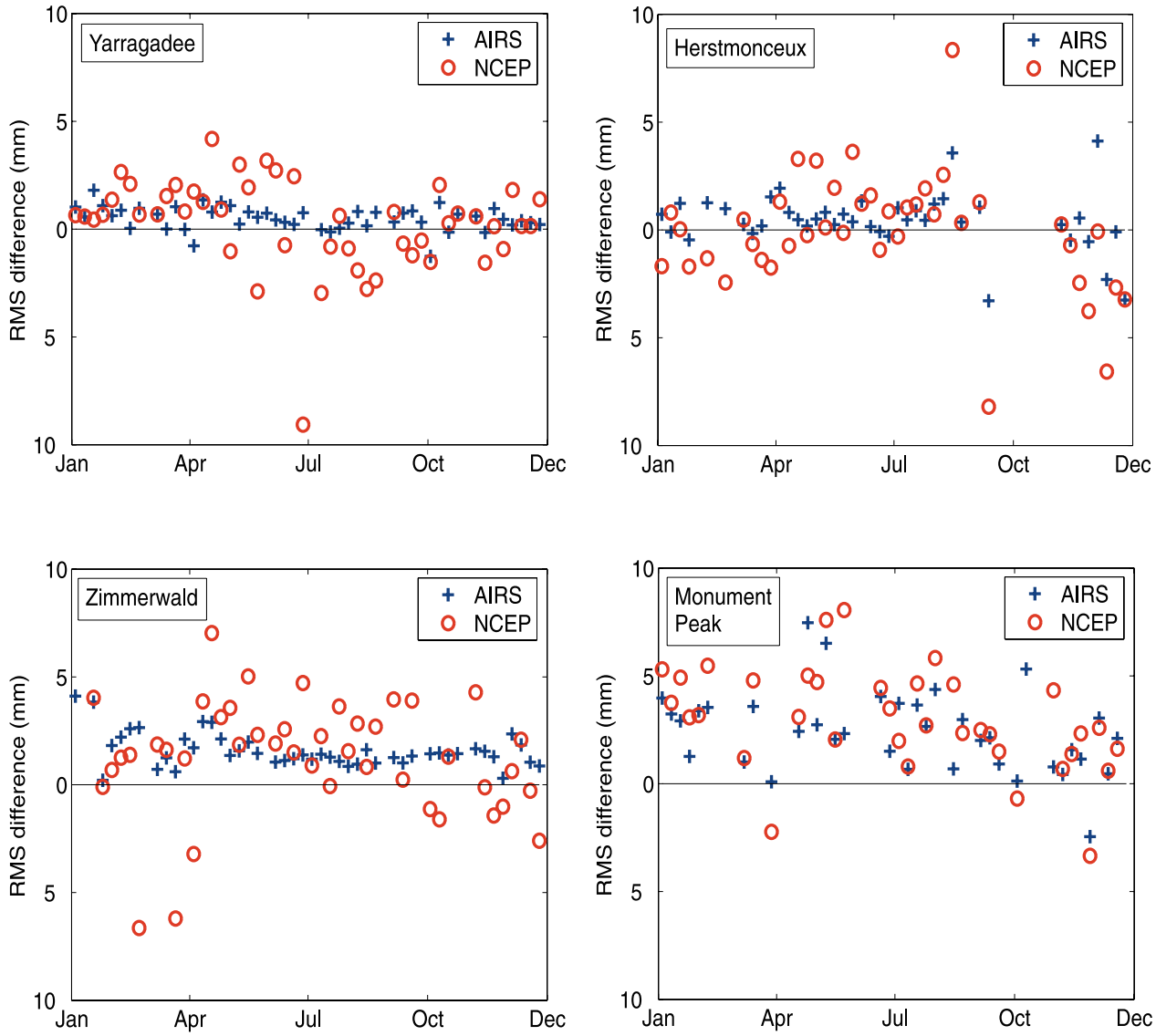

Figure 13. RMS differences for the total-corrected residuals using AIRS and NCEP ray tracing for each weekly arc during the year 2004. Gaps in the data indicate there were no observations for the particular station at that time. Positive values indicate improvement in the results.

tive, constant RMS differences between 0 and 4 mm for all data sources.

8. Conclusions

[59] Our study addresses the contribution of horizontal refractivity gradients to the computation of the total atmospheric delay. We accomplish this by direct ray tracing through three-dimensional atmospheric fields generated using AIRS and NCEP data. We are able to calculate horizontal gradient delays at any selected azimuth, elevation angle, and at any given location on the globe. Our ray-tracing program is tailored for using input atmospheric profiles from AIRS and NCEP, and we make two-way comparisons at 10 of the most prolific, globally distributed ILRS stations during 2004 and 2005.

[60] Our results at 10 SLR stations show that AIRS north-south (NS) and east-west (EW) gradients have annual means of between 1 and 4 mm in absolute magnitude at 10° elevation. The NS component had larger standard deviations ranging from 6 to 12 mm, while the EW component standard deviations were between 5 and 9 mm at all the stations analyzed. Maximum NS gradient delays of up to 50 mm were found at Yarragadee and Herstmonceux at 10° elevation.

[61] From our results in Table 6 we found that the largest variations occur as a result of seasonal and diurnal changes. Stations situated in mountainous regions, such as McDonald and Monument Peak, had larger horizontal pressure gradients while stations in close proximity to large bodies of water (for example, Yarragadee) had larger horizontal temperature gradients. No significant nonhydrostatic (wet) gradients were found, with maximum wet delays only reaching a

few tenths of a millimeter during the summer at Greenbelt. We found that the gradient delays decreased by a factor of 3 from 10° to 20° elevation and were at submillimeter levels at higher elevation angles. The NS and EW gradients varied primarily by station location and time of year. Gradient variations in the NS and EW directions increased from winter to summer at Yarragadee and Monument Peak and from summer to winter at Herstmonceux and Zimmerwald.

[62] By using uncertainties in the most recent AIRS validation results, we were able to estimate error variations in our gradient delay results. We found monthly RMS differences (original minus simulated data) of less than 5 mm for an elevation angle of 10° at Herstmonceux and Yarragadee. Actual day-to-day variations in the gradients were larger and ranged from 7 to 14 mm. Therefore AIRS data is accurate enough to estimate daily changes in horizontal refractivity gradients at the centimeter level.

[63] The effects of replacing the M-P delay model with ray-tracing results in order to calculate the total atmospheric correction (including gradients) resulted in reducing the variance of the SLR observation residuals for LAGEOS 1 and 2 by between 25–43% for NCEP and 10–30% for AIRS during 2004 and 2005. However, NCEP had much larger biases than AIRS at most stations, and an optimum solution will need to be developed in order to extract the best results for future corrections. The improvements shown here will make a highly significant contribution for the SLR technique's effort to develop future ITRFs with an origin accurate to 1 mm at its epoch of definition and a stability of 0.1 mm/year this decade. Future work will involve using a three-dimensional ray-tracing technique to estimate the total delay, and looking at the feasibility of incorporating in a near-real time operational mode several meteorological data sets (AIRS, ECMWF, NCEP, and possibly MetOp in the future), for increased spatiotemporal resolution and improved weekly SLR products.

[64] **Acknowledgments.** We gratefully acknowledge the support from NASA's Cooperative Agreement with JCET NCC5-339 and NGA's Grant NURI NMA201-01-BAA-2002. We also thank the International Laser Ranging Service (ILRS) for making the satellite laser ranging data collected by their network available to us through their data service at CDDIS, NASA/Goddard, USA and the European Data Center at DGFI, Germany.

References

Abshire, J. B., and C. S. Gardner (1985), Atmospheric refractivity corrections in satellite laser ranging, *IEEE Trans. Geosci. Remote Sens.*, *GE-23*(4), 414–425.

Altamimi, Z., P. Sillard, and C. Boucher (2002), ITRF2000: A new release of the International Terrestrial Frame for earth science applications, *J. Geophys. Res.*, *107*(B10), 2214, doi:10.1029/2001JB000561.

Boehm, J., and H. Schuh (2006), Linear horizontal gradients of refractivity vs. 3D raytracing, in International VLBI Service for Geodesy and Astrometry 2006 General Meeting Proceedings, edited by D. Behrend and K. Baver, NASA/CP-2006-214140.

Chen, G. E., and T. A. Herring (1997), Effects of atmospheric azimuthal asymmetry on the analysis of space geodetic data, *J. Geophys. Res*, *102*, 20,489–20,502.

Ciddor, P. E. (1996), Refractive index of air: New equations for the visible and near infrared, *Appl. Opt.*, *35*, 1566–1573.

Ciddor, P. E., and R. J. Hill (1999), Refractive index of air: 2. Group index, *Appl. Opt.*, *38*, 1663–1667.

Davis, J. L., G. Elgered, A. E. Niell, and C. E. Kuehn (1993), Ground-based measurements of gradients in the wet refractive index of air, *Radio Sci.*, *28*, 1003–1018.

Gardner, C. S. (1977), Correction of laser tracking data for the effects of horizontal refractivity gradients, *Appl. Opt.*, *16*(9), 2427–2432.

Gardner, C. S., J. R. Rowlett, and B. E. Hendrickson (1978), Ray tracing evaluation of a technique for correcting the refraction errors in satellite tracking data, *Appl. Opt.*, *17*(19), 3143–3145.

Hauser, J. P. (1991), Effects of deviations from hydrostatic equilibrium on atmospheric corrections to satellite and lunar laser range measurements, *J. Geophys. Res.*, *94*, 10,182–10,186.

International Union of Geodesy and Geophysics (1999), Resolution 3 of the international association of geodesy, Comptes Rendus of the XXII General Assembly, pp. 110–111.

Kalnay, E., et al. (1996), The NCEP/NCAR 40-year reanalysis project, *Bull. Am. Meteorol. Soc.*, *77*, 437–471.

Luthcke, S. B., N. P. Zelensky, D. D. Rowlands, F. G. Lemoine, and T. A. Williams (2003), The 1-centimeter orbit: Jason-1 precision orbit determination using GPS, SLR, DORIS, and altimeter data, *Mar. Geod.*, *26*, 399–421.

MacMillan, D. S. (1995), Atmospheric gradients from Very Long Baseline Interferometry observations, *Geophys. Res. Lett.*, *22*, 1041–1044.

MacMillan, D. S., and C. Ma (1997), Atmospheric gradients and the VLBI terrestrial and celestial reference frames, *J. Geophys. Res.*, *24*, 453–456.

Mendes, V. B., and E. C. Pavlis (2004), High-accuracy zenith delay prediction at optical wavelengths, *Geophys. Res. Lett.*, *31*, L14602, doi:10.1029/2004GL020308.

Mendes, V. B., G. Prates, E. C. Pavlis, D. E. Pavlis, and R. B. Langley (2002), Improved mapping functions for atmospheric refraction correction in SLR, *Geophys. Res. Lett.*, *29*(10), 1414, doi:10.1029/2001GL014394.

Mo, K. C., X. L. Wang, R. Kistler, M. Kanamitsu, and E. Kalnay (1994), Impact of satellite data on the CDAS-reanalysis system, *Mon. Weather Rev.*, *123*, 124–139.

Parker, D. E., T. P. Legg, and C. K. Folland (1992), A new daily central England temperature series, 1772–1991, *Int. J. Climatol.*, *12*, 317–342.

Paros, J., and M. Yilmaz (2002), Broadband meteorological sensors co-located with GPS receivers for geophysical and atmospheric measurements, presented at IEEE PLANS.

Pavlis, D. E., et al. (1998), Geodyn systems description, vol. 3, NASA Goddard, Greenbelt, MD.

Randel, W. J., F. Wu, and D. J. Gaffen (2000), Interannual variability of the tropical tropopause derived from radiosonde data and NCEP reanalyses, *J. Geophys. Res.*, *105*(D12), 15,509–15,524, doi:10.1029/2000JD900155.

Thépaut, J. N. (2003), Satellite data assimilation in numerical weather predicition: An overview, paper presented at the 2nd GRAS SAF User Workshop, Denmark, 11-13 Jun.

G. C. Hulley, Joint Center for Earth Systems Technology, University of Maryland Baltimore County, 1000 Hilltop Circle, Baltimore, MD, USA. (ghulley1@umbc.edu)

E. C. Pavlis, Joint Center for Earth Systems Technology, NASA Goddard Space Flight Center, Greenbelt, MD, USA. (epavlis@umbc.edu)